


Giant Perpendicular Magnetic Anisotropy Enhancement in MgO-Based Magnetic Tunnel Junction by Using Co/Fe Composite Layer

Libor Vojáček^{1,2,*}, Fatima Ibrahim¹, Ali Hallal¹, Bernard Dieny¹, and Mairbek Chshiev^{1,3,†}

¹Univ. Grenoble Alpes, CNRS, CEA, Spintec, 38000 Grenoble, France

²CEITEC BUT, Brno University of Technology, Purkynova 123, 612 00 Brno, Czech Republic

³Institut Universitaire de France (IUF), 75231 Paris Cedex 5, France

 (Received 17 August 2020; revised 8 December 2020; accepted 8 December 2020; published 8 February 2021)

Magnetic tunnel junctions with perpendicular anisotropy form the basis of the spin-transfer torque magnetic random-access memory (STT MRAM), which is nonvolatile, fast, dense, and has quasi-infinite write endurance and low power consumption. Based on density-functional-theory (DFT) calculations, we propose an alternative design of magnetic tunnel junctions comprising $\text{Fe}(n)\text{Co}(m)\text{Fe}(n)|\text{MgO}$ storage layers [n and m denote the number of monolayers (ML)] with greatly enhanced perpendicular magnetic anisotropy (PMA) up to several mJ/m^2 , leveraging the interfacial perpendicular anisotropy of $\text{Fe}|\text{MgO}$ along with a strain-induced bulk PMA discovered within bcc Co. This giant enhancement dominates the demagnetizing energy when increasing the film thickness. The tunneling magnetoresistance (TMR) estimated from the Julliere model is comparable with that of the pure $\text{Fe}|\text{MgO}$ case. We discuss the advantages and pitfalls of a real-life fabrication of the structure and propose the $\text{Fe}(3\text{ML})\text{Co}(4\text{ML})\text{Fe}(3\text{ML})$ as a storage layer for MgO-based STT MRAM cells. The large PMA in strained bcc Co is explained in the framework of second-order perturbation theory by the MgO-imposed strain and consequent changes in the energies of d_{yz} and d_{z^2} minority-spin bands.

DOI: [10.1103/PhysRevApplied.15.024017](https://doi.org/10.1103/PhysRevApplied.15.024017)

I. INTRODUCTION

MgO-based magnetic tunnel junctions (MTJs) are used in today's hard-disk-drive read heads and a variety of magnetic field sensors for their supremely high tunneling magnetoresistance (TMR) effect [1]. Hard-disk drives, however, are approaching their scaling limits [2]. Besides, spin-transfer torque magnetic random-access memory (STT MRAM), also based on MTJs comprising an MgO tunnel barrier, is entering into volume production for eFLASH replacement and SRAM type of applications. They are nonvolatile, fast (5–50 ns cycle time), can be made relatively dense (Gbit), with low power consumption (100 fJ/write event), and exhibit very good write endurance [3–5].

The building block of STT MRAM is a cell with (1) high TMR for good readability, (2) high spin-transfer torque efficiency for good writability, and (3) high magnetic anisotropy for good thermal stability and therefore memory retention [6,7]. All of these requirements must be satisfied together, which is the case in perpendicularly magnetized Co-Fe-B|MgO MTJs as long as the cell diameter remains larger than approximately 30 nm [8].

Below this diameter, the perpendicular anisotropy provided by the Co-Fe-B|MgO interface becomes too weak in regards to thermal fluctuations so that the memory retention reduces excessively. In this work, we focus on improving the third requirement—the perpendicular magnetic anisotropy (PMA)—of the MgO-based MTJ, therefore allowing improved downsize scalability of out-of-plane magnetized MRAM.

Although heavy metals like Pt or Pd can enhance PMA [9,10], they do so by increasing the spin-orbit coupling (SOC) parameter ξ . This is, however, associated with the undesirable side effect of increasing the Gilbert damping [11], thus increasing the spin-transfer torque switching current [12,13]. To avoid this problem, recipes based on purely $3d$ metallic elements were developed [14,15]. However, these recipes are based on Fe/Ni or Co/Ni alternating atomic layers, yielding structures that are intrinsically complex to fabricate or may require excessively high deposition or annealing temperature. They can also get deteriorated upon the annealing necessary to obtain good crystallization of the MgO barrier and surrounding magnetic electrodes.

In this work, we propose a different approach based on introducing a bulk Co interlayer into a simple $\text{Fe}|\text{MgO}$ MTJ. The latter exhibits comparable or stronger PMA than the aforementioned Fe/Ni or Co/Ni alternating atomic

*libor.vojacek@vutbr.cz

†mair.chshiev@cea.fr

layers. In addition, the PMA characterized by the magnetocrystalline anisotropy energy E_{MCA} increases with the film thickness at a comparable or higher rate. Lastly, the Co Curie temperature (1404 K) is significantly higher than that of Fe (1043 K) and twice higher than that of Ni (631 K), which provides higher temperature stability [16].

The paper is organized as follows. In Sec. II, based on DFT calculations, we propose a MTJ with enhanced PMA and high TMR and discuss the aspects useful for a real-life fabrication of the structure. In Sec. III, the systematic calculations supporting our proposal are presented. In Sec. IV, the large bulk Co|MgO PMA, crucial to the enhancement, is explained by the electronic structure and the second-order perturbation theory.

II. MTJ WITH GREATLY ENHANCED PMA

The DFT calculations are performed using the Vienna *ab initio* simulation package (VASP) [17,18]. Besides the electronic structure, the primary output of the calculations is the magnetocrystalline anisotropy energy E_{MCA} and its atomic site-resolved contributions. Positive (negative) value of E_{MCA} indicates PMA (in-plane anisotropy), respectively. See the Supplemental Material [19] for calculation details [20–22].

A. PMA enhancement

In this study, we find that a significant contribution to PMA originates from the bulk of epitaxial bcc Co on top of MgO. Its origin is presented in detail in Secs. III and IV. We exploit this finding and propose to enhance the PMA of conventional Fe|MgO MTJ by replacing the bulk Fe layers with Co. The effect can be further enhanced by sandwiching the magnetic layer between two MgO barriers. The proposed improved MTJ storage layer thus takes the form MgO|Fe(n)Co(m)Fe(n)|MgO with $n \geq 2$ and $m \geq 3$, as shown in Fig. 1(c). It is required to have at least two Fe atoms at the MgO interface and three successive Co atoms in the bulk to obtain the PMA enhancement (see Fig. S1 within the Supplemental Material [19] for details).

Structures with different n and m are systematically investigated. The thickness of MgO in all the calculations is chosen to be 5 (6) monolayers for an odd (even) number of metal layers, respectively. Figure 1(a) shows the effective PMA, which is a sum of the magnetocrystalline anisotropy energy E_{MCA} and dipole-dipole-induced demagnetization energy E_{DD} as a function of n , m . One can see that the effective PMA does not vanish with increasing thickness, but interestingly, it grows steadily. This contrasts with the pure Fe|MgO case (gray line), where the demagnetizing energy E_{DD} drives the magnetization in plane for thicknesses above 11 monolayers. The variation of E_{MCA} and E_{DD} as a function of m for $n = 2$ is shown in Fig. 1(b).

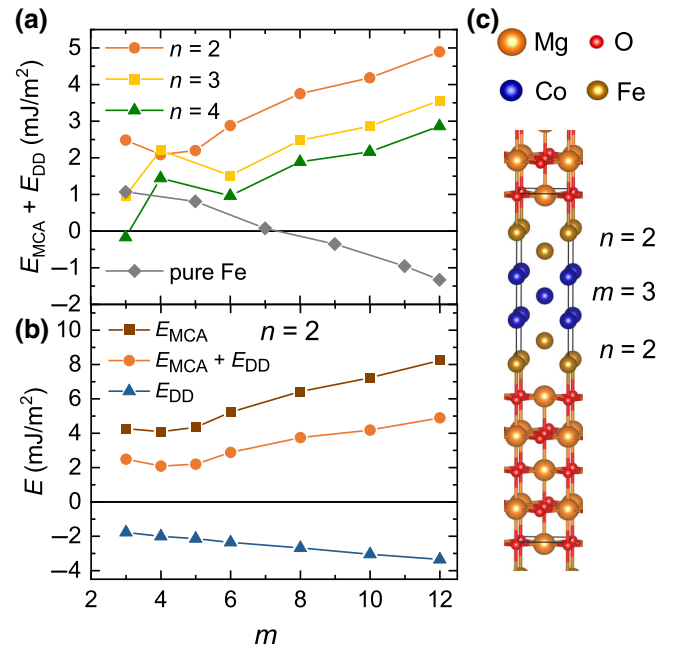


FIG. 1. (a) Effective PMA ($E_{MCA} + E_{DD}$) in MgO|Fe(n)Co(m)Fe(n)|MgO as a function of number of monolayers n , m . There is no perpendicular to in-plane magnetic anisotropy switching compared to pure MgO|Fe|MgO (gray diamonds; its thickness is $m+4$ ML, the same as the overall thickness for $n = 2$). (b) E_{MCA} , E_{DD} , and the effective PMA ($E_{MCA} + E_{DD}$) for $n = 2$. The effective PMA increases with the Co thickness. (c) Supercell of the MgO|Fe(2)Co(3)Fe(2)|MgO with periodic boundary conditions applied in all directions. Produced by VESTA [23].

The dipole-dipole energy E_{DD} is obtained by summing over all the dipole-dipole interactions [24,25] (see the Supplemental Material [19] for calculation details). E_{DD} acts mainly as demagnetizing energy [24], favoring an in-plane magnetization orientation. E_{DD} is proportional to the product of the magnetic moments of the interacting atoms ($\mu_1 \cdot \mu_2$). Thus, replacing the bulk Fe with Co decreases its magnitude knowing that in the bulk of the layer $\mu_{Fe} \approx 2.5\mu_B$ while $\mu_{Co} \approx 1.8\mu_B$, where μ_B is the Bohr magneton. The effect of the bulk Co is therefore twofold: it increases the positive E_{MCA} (discussed in detail in Secs. III and IV) and diminishes the negative demagnetizing dipole-dipole contribution.

Replacing the MgO on one side of the metal film with vacuum, as tested on the $n = 4$, $m = 6$ structure, decreases the E_{MCA} by 16% (see the Supplemental Material [19]). This is predominantly due to the drop in E_{MCA} of the two interfacial Fe atoms [26]. (The effect of replacing the MgO by vacuum in pure bcc Fe(Co, Ni)|MgO can also be seen in Fig. S3 within the Supplemental Material [19].) However, at reduced thicknesses ($n = 2$, $m = 3$), this drop is much more dramatic, namely 36%, or even 86%, when both interfaces are in contact with vacuum. This explains why

Hotta *et al.* [14] observed no enhancement of anisotropy in Fe(2)Co(3)Fe(2)|MgO. They mimicked the presence of MgO by setting the lattice parameter equal to that of bulk MgO while, in reality, having vacuum at the interfaces.

Note that changing the MgO thickness from 3 ML to 7 ML has a negligible effect on the E_{MCA} in the order of 0.01 mJ/m^2 , as tested on the Fe(2)Co(3)Fe(2).

B. Tunneling magnetoresistance

Since we are interested in implementing this proposed storage layer in a full MTJ stack, we investigate its expected TMR amplitude. A large TMR of 410% at room temperature has been observed previously in pure bcc Co|MgO|Co MTJs [27]. In addition, Co in combination with Fe is often used for its record-holding TMR values. Therefore, we expect the high TMR to be present also in the proposed Fe|MgO MTJs with the inserted Co bulk layer. We estimate the TMR of the structures from the Julliere formula [28] with the spin polarization calculated from the local density of states with Δ_1 symmetry of the interfacial oxygen at the Fermi level. The values are very high, around 300%. Note that the PMA does not originate solely from the interface in the proposed structure, but also from the bulk, in contrast to pure Fe|MgO [26]. This suggests that we might be able to separately tune the PMA (by the bulk Co) and the TMR (by the Fe|MgO interface).

As mentioned in the introduction, the proposed MTJ is conceptually much simpler and more robust against annealing than the alternating layer-based MTJ [14,15] with similar properties. However, there are two main issues that we address regarding the fabrication of our structure, namely the stability of the bcc Co phase and the robustness against the Fe-Co interface not being atomically sharp.

C. Fabrication of the metastable bcc Co

Although the natural form of Co is hcp, the metastable bcc Co phase can be grown at room temperature [29–31]. It has been successfully grown on top of Fe with thickness up to 15 ML [32], with well-defined interfaces and no visible interdiffusion. The observed strain of 10% in bcc Co|MgO is considerable but still within the limit of what is experimentally realizable [33]. Indeed, Yuasa *et al.* [27] fabricated bcc Co(4ML)|MgO(10ML)|Co(4ML) MTJ and measured a record-holding TMR of 410% at room temperature. From our structural relaxation simulations, it follows that the bcc Co is preserved on top of MgO while it transforms into the fcc phase when surrounded by vacuum. Therefore, the bcc phase will probably be most stable if the device is used as a double-barrier MTJ. This also provides higher PMA from the interfacial Fe, compared to single-barrier MTJ.

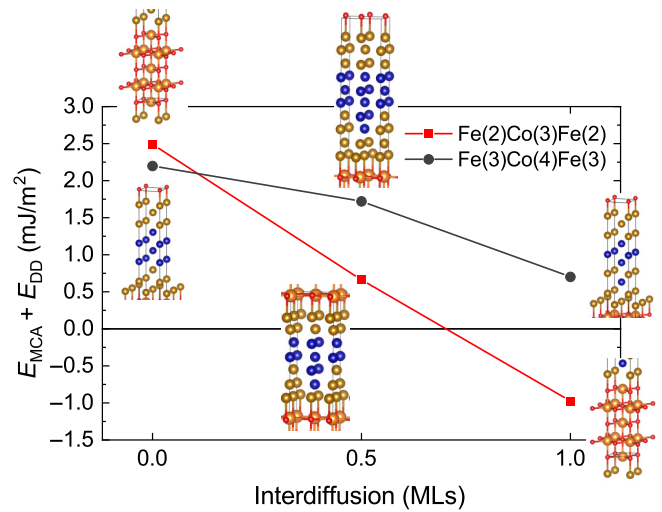


FIG. 2. The effect of interdiffusion on the effective PMA in two selected structures. For the (minimal) Fe(2)Co(3)Fe(2) structure, there is a significant PMA decrease of 73% at 0.5-ML atomic intermixing. For the thicker Fe(3)Co(4)Fe(3), the PMA is reduced only by 22%, demonstrating the robustness against interfacial roughness. We expect this robustness in the thicker structures in general.

D. Decrease of PMA with interfacial roughness

The sharpness of the Fe-Co interface is another relevant factor to consider. From the simulations it follows that any interdiffusion is fatal for the PMA when the Fe or Co thickness is less than 2 ML or 3 ML, respectively ($n < 2$ or $m < 3$; see Fig. S1 within the Supplemental Material [19]). Robustness can be achieved at larger Fe and Co thicknesses. In Fig. 2, one may see the effective PMA in the Fe(2)Co(3)Fe(2) and Fe(3)Co(4)Fe(3) structures with 0.5-ML (50%) interdiffusion and when the interface layers are swapped (1-ML interdiffusion). The drop in the effective PMA of Fe(3)Co(4)Fe(3) is only 22% at 0.5-ML interdiffusion, compared to a drop of 73% for Fe(2)Co(3)Fe(2). This robustness against surface roughness is to be expected in the thicker structures in general.

Larger Co thickness is favorable as it increases the PMA (Fig. 1), but on the other hand, thicker bcc Co will probably be harder to fabricate [27]. Larger Fe thickness provides robustness against interdiffusion and might stabilize the bcc Co, as it is generally easier to grow bcc Co on Fe than on MgO (Co does not wet well on oxides due to its high surface tension while Fe does [34,35]). On the other hand, the PMA is decreased with thicker Fe, as shown in Fig. 1(a) (for layer-resolved behavior, see Fig. S4 within the Supplemental Material [19]).

Looking at Fig. 1(a) and considering all the mentioned aspects, the MgO|Fe(3ML)Co(4ML)Fe(3ML)|MgO seems like a promising candidate as a storage layer for STT MRAM cells with highly improved thermal stability

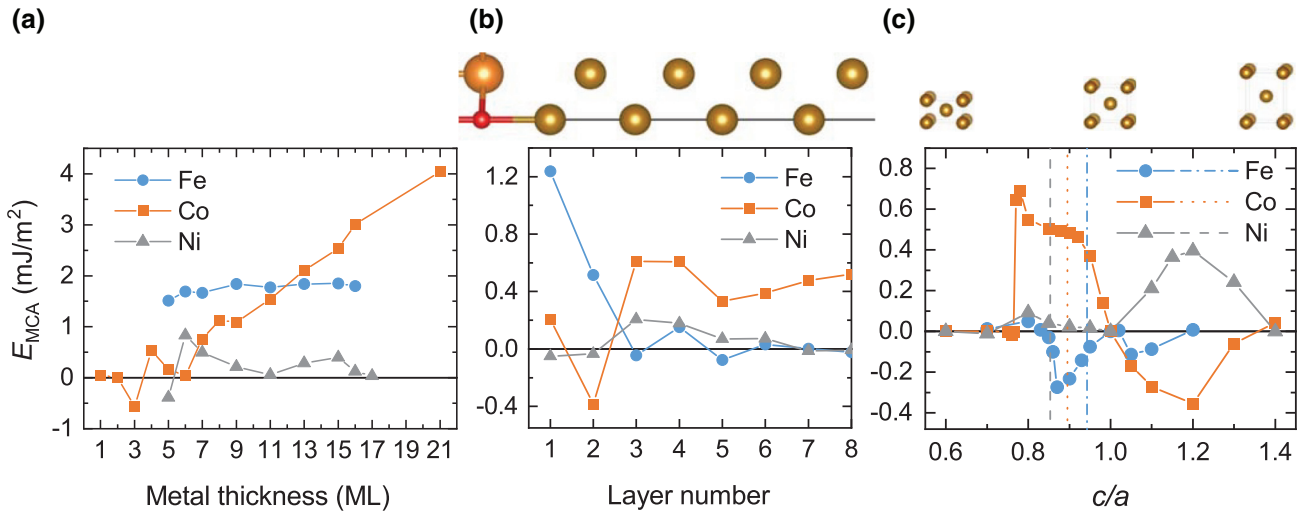


FIG. 3. (a) Thickness dependence of E_{MCA} in bcc Fe(Co, Ni)|MgO. Surprisingly, the PMA in Co increases steadily. (b) Layer-resolved E_{MCA} in the structure with 15 ML of metal. Layer 1 is the interfacial layer. The layer number increases towards the bulk of the material. The largest contribution for Fe comes from the interface; for Co, it comes from the bulk. (c) E_{MCA} in purely bulk bcc Fe, Co, and Ni as a function of c/a ratio. Dashed lines indicate the typical value of c/a in the bulk of the given metal|MgO (see text for details). At its typical strain, the E_{MCA} for Co is the same as in the bulk layers in Fig. 3(b).

compared to conventional STT MRAM. Indeed, when the storage layer is sandwiched between two MgO layers, the anisotropy per unit area is of the order of $2 \text{ mJ}/\text{m}^2$ from the interfacial contribution minus approximately $1.2 \text{ mJ}/\text{m}^2$ from demagnetizing energy (dependent on the chosen storage layer thickness) yielding a net effective PMA per unit area approximately $0.8 \text{ mJ}/\text{m}^2$ [4]. In comparison, the net anisotropy per unit area in the proposed structure is approximately $2.2 \text{ mJ}/\text{m}^2$ being almost 3 times larger. This means that for the same thermal stability factor, the cell area could be reduced by a factor of 3 compared to conventional MRAM [7,36].

III. PMA IN BCC Fe(Co, Ni)|MgO THIN FILMS

The idea of the improved MTJ proposed above is driven by our systematic investigation of the thickness dependence of E_{MCA} in pure bcc (001) Fe, Co, and Ni|MgO ultrathin films. The E_{MCA} as a function of metallic layer thickness is presented in Fig. 3(a). While for Fe the E_{MCA} converges to a constant value [26], we observe a steady increase for Co. The behavior for Ni is more subtle. To elucidate why the trend varies among the three metals, in Fig. 3(b), we show the layer-resolved contributions to the E_{MCA} (the contributions from each atomic layer separately).

For Fe, the main contribution to E_{MCA} comes from the first two interfacial layers [26,37]. Increasing the thickness does not affect the electronic properties of the interfacial layers in a significant way [26] (see also Fig. S5 within the Supplemental Material [19]). The bulk layers almost do not contribute to the PMA. Hence the E_{MCA} does not change.

In contrast, all the bulk layers of Co seem to contribute with a significant positive E_{MCA} value, as evident from Fig. 3(b). Hence, the E_{MCA} grows almost linearly with the number of added bulk Co layers [see Fig. 3(a)]. This observation is the cornerstone of this paper.

For Ni, the influence of the interface manifests itself as deep as 6 ML, with the two interfacial monolayers contributing a negative E_{MCA} . This is the reason for the in-plane anisotropy in the 5-ML structure, as shown in Fig. 3(a). Although the deeper bulk layers contribute positively, the E_{MCA} does not grow monotonically as expected because the interfacial contributions in Ni do change upon thickness increase (see Fig. S5 in the Supplemental Material [19]). The bcc Ni|MgO is problematic also because of the large strain of approximately 15%.

The large positive bulk E_{MCA} in Co|MgO is caused by the strain that is induced within the Co by the MgO. To confirm this hypothesis, we have calculated E_{MCA} as a function of the c/a ratio in the primitive bcc unit cell for each of the metals shown in Fig. 3(c). The a and b lattice parameters were set to the value of the relaxed bulk bcc Fe, Co, or Ni unit cell, while the c lattice parameter was varied. The typical relaxed c/a ratios we found within the bulk metal layers in Fe, Co, and Ni interfaced with MgO are 0.94, 0.89, and 0.85, respectively [dashed lines in Fig. 3(c)].

It clearly follows from Fig. 3(c) that for Fe and Ni, this bulk strain-induced E_{MCA} is very small at their typical bulk strains (dashed lines). However, we observe a large positive contribution of $\approx 0.5 \text{ mJ}/\text{m}^2$ for Co, which is the same value expected from Fig. 3(b). Indeed, artificially setting $c/a = 1$ in a previously relaxed Co|MgO

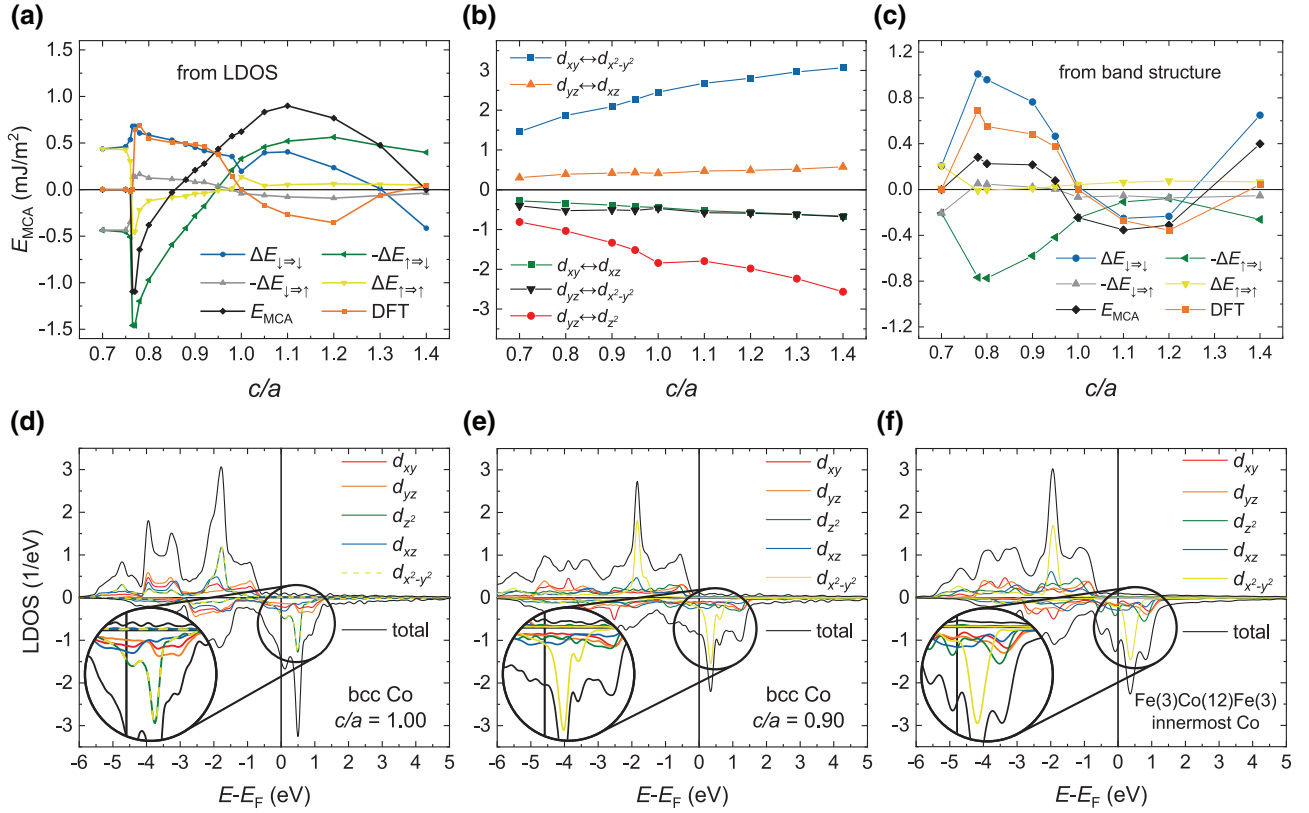


FIG. 4. (a) Based on the orbital-resolved local density of states, the four contributions to the bcc Co $E_{MCA}(c/a)$ calculated from the second-order perturbation theory [41] are shown separately and in total. The values extracted from the DFT calculation with spin-orbit coupling included [“DFT”; see Fig. 3(c)] are shown for comparison. The classical Bruno term $\Delta E_{\downarrow\rightarrow\downarrow}$ on its own reproduces the DFT curve for $c/a < 1$ to a certain extent. (b) The Bruno $\Delta E_{\downarrow\rightarrow\downarrow}$ term from Fig. 4(a) divided into contributions from individual virtual excitations. The excitation from d_{yz} to d_{z^2} states and vice versa ($d_{yz} \leftrightarrow d_{z^2}$; red circles) is the one that causes the overall increase for $c/a < 1$. (c) Same as Fig. 4(a) but calculated from the orbital-projected band structure, where additional aspects are taken into account (see text for details). The correspondence with the DFT curve is hence much better. (d) The orbital-resolved DOS for bcc Co with $c/a = 1$. There is a peak in the d_{z^2} and $d_{x^2-y^2}$ minority states right above the Fermi level. (e) The orbital-resolved DOS for bcc Co with $c/a = 0.90$. The strain causes the overall spreading of the DOS. Both the d_{z^2} and the $d_{x^2-y^2}$ peaks are pushed further above E_F . (f) The most bulklike Co from the Fe(3)Co(12)Fe(3) structure. Its features are very similar to the bcc Co with $c/a = 0.90$ in Fig. 4(e), supporting the applicability of the results of Sec. IV to the proposed structures of Sec. II.

eliminates the bulk contribution to E_{MCA} , thus confirming that strain plays the central role. We note that the calculated $E_{MCA}(c/a)$ dependence in Fig. 3(c) corresponds well to previous findings [38,39], where the focus was limited to $c/a > 1$.

IV. PERTURBATIVE TREATMENT OF STRAIN-INDUCED ANISOTROPY IN BCC COBALT

The magnetocrystalline anisotropy is due to the spin-orbit coupling [40]. The magnitude of spin-orbit coupling constant is several 10 meV, which is much less than the width of $3d$ bands. Therefore, the E_{MCA} can be calculated within the second-order perturbation theory framework directly from the orbital-resolved (A) density of states or (B) band structure. Both of these are obtained from a DFT

calculation with the spin-orbit coupling not included. This treatment allows us to link changes in E_{MCA} directly to changes in the electronic structure.

A. Density of states

The magnetic anisotropy energy can be calculated from the local density of states (LDOS) at a particular atom as [41]

$$E_{MCA} = \Delta E_{\downarrow\rightarrow\downarrow} + \Delta E_{\uparrow\rightarrow\uparrow} - \Delta E_{\uparrow\rightarrow\downarrow} - \Delta E_{\downarrow\rightarrow\uparrow}, \quad (1)$$

where [42]

$$\Delta E_{\sigma\Rightarrow\sigma'} = \frac{\xi^2}{4} \sum_{\mu\mu'} P_{\mu\mu'} \int_{-\infty}^{E_F} d\varepsilon \int_{E_F}^{\infty} d\varepsilon' \frac{\rho_{\mu}^{\sigma}(\varepsilon) \rho_{\mu'}^{\sigma'}(\varepsilon')}{\varepsilon' - \varepsilon}. \quad (2)$$

Here ξ is the spin-orbit coupling constant, μ (μ') is an occupied (unoccupied) orbital with spin σ (σ') and density of states ρ_μ^σ ($\rho_{\mu'}^{\sigma'}$) at energy ε (ε'). The constant $P_{\mu\mu'} = |\langle \mu | L_z | \mu' \rangle|^2 - |\langle \mu | L_x | \mu' \rangle|^2$, where L_z (L_x) is the orbital momentum operator in the out-of-plane (in-plane) direction, respectively. The $P_{\mu\mu'}$ matrix for d orbitals is given in the Supplemental Material [19]. We use $\xi_{\text{Co}} = 84$ meV [43].

The physical picture encompassed in Eqs. (1) and (2) is that virtual excitations of electrons from occupied to unoccupied orbitals give rise to positive, negative, or zero contribution to E_{MCA} . The sign depends on the $P_{\mu\mu'}$ constant, and hence on the two interacting orbitals μ and μ' . The closer the two orbitals are to each other, and hence to the Fermi level E_F , and the larger their density of states ρ , the larger this contribution. The excitations are divided into four terms [Eq. (2)] based on the orbitals' spins. The two "spin-conservation terms" have a plus sign, while the two "spin-flip terms" have a minus sign.

In Fig. 4(a), we aim to reproduce the DFT-calculated results from Fig. 3(c) using the model from Eqs. (1) and (2). We show the four terms from Eq. (1), their sum (" E_{MCA} "), and the Co DFT curve from Fig. 3(c) for comparison ("DFT"). The E_{MCA} curve does not reproduce the DFT curve well, so the model from Eq. (2) must be an oversimplification. Despite this, we can use it to draw several qualitative conclusions.

(1) The minority-to-minority excitation term $\Delta E_{\downarrow \Rightarrow \downarrow}$ (the only term that is taken into account in the original Bruno approach [40]) on its own can reproduce the increase of E_{MCA} for $c/a < 1$ observed in the DFT curve. To link this increase directly to changes in the LDOS in Fig. 4(d), in Fig. 4(b), we show all the excitations contributing to $\Delta E_{\downarrow \Rightarrow \downarrow}$ separately. We see that the increase is caused by excitations from d_{yz} to d_{z^2} minority orbitals and vice versa ($d_{yz} \leftrightarrow d_{z^2}$). This is linked to the strain-induced changes in the LDOS: for $c/a < 1$ [Fig. 4(e)], the d_{z^2} peak in the unoccupied minority states is shifted further above the Fermi level, diminishing the negative $d_{yz} \rightarrow d_{z^2}$ contribution. This increases the overall E_{MCA} . The increase is counteracted by a decrease in the positive $d_{xy} \leftrightarrow d_{x^2-y^2}$ excitation contribution. This decrease is due to the strain-induced shift of the minority unoccupied $d_{x^2-y^2}$ peak, located immediately above E_F for $c/a = 1$.

(2) The two contributions that come from excitations to majority-spin states, $\Delta E_{\uparrow \Rightarrow \uparrow}$ and $-\Delta E_{\downarrow \Rightarrow \uparrow}$, are small. The reason is that there are almost no unoccupied majority-spin states, especially near the Fermi level, as we see in Figs. 4(d)–4(f). Moreover, these two contributions tend to cancel each other. Hence they can often be neglected [42].

Note that including the p orbitals gives only a minor correction of approximately 1%.

B. Band structure

Next, we calculate the $E_{\text{MCA}}(c/a)$ directly from the (orbital-resolved) band structure [Eqs. (4)–(6) in [41]]. This approach intrinsically includes many aspects that are neglected in the calculation from LDOS in Sec. IV A, namely that (1) the projection coefficient of a Bloch state onto a particular d orbital is a complex number, (2) virtual excitations also happen in between atoms at different sites, not only on site, and that (3) a virtual excitation generally includes four orbitals, not only two (see Fig. 1 in Ref. [44]). All of these have proven to be essential for the model to be more accurate.

The whole calculation is nicely described by Miura *et al.* [41]. In short, setting LORBIT = 12 in the VASP calculation provides the real and imaginary parts of the projection coefficients c , which we use to calculate the joint local density of states G (see Ref. [41]). Taking its real part and performing summation over several variables, one may obtain the four contributions to E_{MCA} from Eq. (1). We use $\xi_{\text{Co}} = 84$ meV [43].

The calculation results are plotted in Fig. 4(c). The model is much better than the one in Fig. 4(a), while the main features are retained, namely that the $\Delta E_{\downarrow \Rightarrow \downarrow}$ term governs the overall trend. The $-\Delta E_{\uparrow \Rightarrow \downarrow}$ term serves to refine the shape, but in addition, causes an excessive overall decrease. The $E_{\text{MCA}}(c/a = 1)$ is not zero in the E_{MCA} curve, as it should be by symmetry arguments and as it is in the DFT curve. Despite that, the difference $E_{\text{MCA}}(c/a = 0.90) - E_{\text{MCA}}(c/a = 1)$ in the E_{MCA} and DFT curves correspond well to each other.

Analyzing the contributions to $\Delta E_{\downarrow \Rightarrow \downarrow}$ from individual excitations, we confirm the results of Sec. IV A, namely that the main positive change in E_{MCA} for $c/a < 1$ is due to the $d_{yz} \rightarrow d_{z^2}$ virtual excitation, and the main negative change is due to the $d_{x^2-y^2} \rightarrow d_{xy}$ excitation.

V. CONCLUSIONS

We propose an alternative concept of MTJ with strongly enhanced perpendicular magnetic anisotropy based on introducing a Co interlayer into the bulk of conventional Fe|MgO MTJ. DFT calculations confirm that the PMA enhancement overcomes the negative demagnetizing energy in these Fe(n)Co(m)Fe(n)|MgO structures. The TMR shows values similar to the pure Fe|MgO case. There is a trade-off between the enhancement magnitude and its robustness against the Fe-Co interfacial diffusion in a prospective real-life fabrication process. The Fe(3ML)Co(4ML)Fe(3ML) seems of strong potential as a storage layer for MgO-based STT MRAM cells. The design is based on the presented systematic study of PMA in bcc Fe(Co, Ni)|MgO, showing clearly that the MgO-imposed compressive strain induces a significant bulk PMA in bcc Co. We explain the PMA enhancement in bcc Co via the second-order perturbation theory approach and

attribute it mainly to the strain-induced changes in energies of the minority-spin filled d_{yz} and unfilled d_{z^2} orbitals around the Fermi level.

ACKNOWLEDGMENTS

Computational resources are partially supplied by the project “e-Infrastruktura CZ” (e-INFRA LM2018140) provided within the program “Projects of Large Research, Development and Innovations Infrastructures”. B.D. acknowledges ERC funding via ERC Adv grant No. MAGICAL 669204. Co-funded by the Erasmus+ Programme of the European Union.

-
- [1] C. H. Bajorek, Magnetoresistive (MR) Heads and the Earliest MR Head-Based Disk Drives: Sawmill and Corsair, Computer History Museum, Mountain View, CA, Tech. Rep. (2014).
- [2] H. J. Richter, Density limits imposed by the microstructure of magnetic recording media, *J. Magn. Magn. Mater.* **321**, 467 (2009).
- [3] J. Meena, S. Sze, U. Chand, and T.-Y. Tseng, Overview of emerging nonvolatile memory technologies, *Nanoscale Res. Lett.* **9**, 526 (2014).
- [4] A. V. Khvalkovskiy, D. Apalkov, S. Watts, R. Chepulskaa, R. S. Beach, A. Ong, X. Tang, A. Driskill-Smith, W. H. Butler, P. B. Visscher, D. Lottis, E. Chen, V. Nikitin, and M. Krounbi, Basic principles of STT MRAM cell operation in memory arrays, *J. Phys. Appl. Phys.* **46**, 074001 (2013).
- [5] Y. Huai, Spin-Transfer torque MRAM (STT MRAM): Challenges and prospects, *AAPPS Bull.* **18**, 8 (2008).
- [6] A. D. Kent, Perpendicular all the way, *Nat. Mater.* **9**, 699 (2010).
- [7] B. Dieny and M. Chshiev, Perpendicular magnetic anisotropy at transition metal/oxide interfaces and applications, *Rev. Mod. Phys.* **89**, 025008 (2017).
- [8] S. Ikeda, K. Miura, H. Yamamoto, K. Mizunuma, H. D. Gan, M. Endo, S. Kanai, J. Hayakawa, F. Matsukura, and H. Ohno, A perpendicular-anisotropy CoFeB-MgO magnetic tunnel junction, *Nat. Mater.* **9**, 721 (2010).
- [9] P. F. Garcia, A. D. Meinhaldt, and A. Suna, Perpendicular magnetic anisotropy in Pd/Co thin film layered structures, *Appl. Phys. Lett.* **47**, 178 (1985).
- [10] S. Hashimoto, Y. Ochiai, and K. Aso, Perpendicular magnetic anisotropy and magnetostriction of sputtered Co/Pd and Co/Pt multilayered films, *J. Appl. Phys.* **66**, 4909 (1989).
- [11] P. Bruno, in *Ferienkurse Des Forschungszentrums Julich* (1993), p. 29.
- [12] S. Mizukami, E. P. Sajitha, D. Watanabe, F. Wu, T. Miyazaki, H. Naganuma, M. Oogane, and Y. Ando, Gilbert damping in perpendicularly magnetized Pt/Co/Pt films investigated by all-optical pump-probe technique, *Appl. Phys. Lett.* **96**, 152502 (2010).
- [13] J. C. Slonczewski, Current-driven excitation of magnetic multilayers, *J. Magn. Magn. Mater.* **159**, L1 (1996).
- [14] K. Hotta, K. Nakamura, T. Akiyama, T. Ito, T. Oguchi, and A. J. Freeman, Atomic-Layer Alignment Tuning for Giant Perpendicular Magnetocrystalline Anisotropy of 3d Transition-Metal Thin Films, *Phys. Rev. Lett.* **110**, 267206 (2013).
- [15] K. Nakamura, Y. Ikeura, T. Akiyama, and T. Ito, Giant perpendicular magnetocrystalline anisotropy of 3d transition-metal thin films on MgO, *J. Appl. Phys.* **117**, 17C731 (2015).
- [16] B. D. Cullity, *Introduction to Magnetic Materials* (Addison-Wesley, Reading, MA, 1972).
- [17] G. Kresse and J. Hafner, Ab initio molecular dynamics for liquid metals, *Phys. Rev. B* **47**, 558 (1993).
- [18] G. Kresse and J. Furthmüller, Efficiency of Ab-initio total energy calculations for metals and semiconductors using a plane-wave basis set, *Comput. Mater. Sci.* **6**, 15 (1996).
- [19] See Supplemental Material at <http://link.aps.org/supplemental/10.1103/PhysRevApplied.15.024017> for additional calculations and description of calculation procedures.
- [20] A. Hallal, B. Dieny, and M. Chshiev, Impurity-induced enhancement of perpendicular magnetic anisotropy in Fe/MgO tunnel junctions, *Phys. Rev. B* **90**, 064422 (2014).
- [21] Y. Wang and J. P. Perdew, Correlation hole of the spin-polarized electron gas, with exact small-wave-vector and high-density scaling, *Phys. Rev. B* **44**, 13298 (1991).
- [22] J. P. Perdew, K. Burke, and M. Ernzerhof, Generalized Gradient Approximation Made Simple, *Phys. Rev. Lett.* **77**, 3865 (1996).
- [23] K. Momma and F. Izumi, *J. Appl. Crystallogr.* **44**, 1272 (2011).
- [24] H. J. G. Draaisma and W. J. M. de Jonge, Surface and volume anisotropy from dipole-dipole interactions in ultrathin ferromagnetic films, *J. Appl. Phys.* **64**, 3610 (1988).
- [25] G. H. O. Daalderop, P. J. Kelly, and M. F. H. Schuurmans, First-Principles calculation of the magnetocrystalline anisotropy energy of iron, cobalt, and nickel, *Phys. Rev. B* **41**, 11919 (1990).
- [26] A. Hallal, H. X. Yang, B. Dieny, and M. Chshiev, Anatomy of perpendicular magnetic anisotropy in Fe/MgO magnetic tunnel junctions: First-principles insight, *Phys. Rev. B* **88**, 184423 (2013).
- [27] S. Yuasa, A. Fukushima, H. Kubota, Y. Suzuki, and K. Ando, Giant tunneling magnetoresistance up to 410% at room temperature in fully epitaxial Co/MgO/Co magnetic tunnel junctions with Bcc Co(001) electrodes, *Appl. Phys. Lett.* **89**, 042505 (2006).
- [28] M. Julliere, Tunneling between ferromagnetic films, *Phys. Lett. A* **54**, 225 (1975).
- [29] H. Li and B. P. Tonner, Direct experimental identification of the structure of ultrathin films of Bcc iron and metastable Bcc and Fcc cobalt, *Phys. Rev. B* **40**, 10241 (1989).
- [30] S. Subramanian, X. Liu, R. L. Stamps, R. Sooryakumar, and G. A. Prinz, Magnetic anisotropies in body-centered-cubic cobalt films, *Phys. Rev. B* **52**, 10194 (1995).
- [31] X. Liu, R. L. Stamps, R. Sooryakumar, and G. A. Prinz, Magnetic anisotropies in thick body centered cubic Co, *J. Appl. Phys.* **79**, 5387 (1996).
- [32] Ph. Houdy, P. Boher, F. Giron, F. Pierre, C. Chappert, P. Beauvillain, K. L. Dang, P. Veillet, and E. Velu, Magnetic and structural properties of Rf-sputtered Co/Fe and Co/Cr multilayers, *J. Appl. Phys.* **69**, 5667 (1991).

- [33] D. Sander, The magnetic anisotropy and spin reorientation of nanostructures and nanoscale films, *J. Phys. Condens. Matter.* **16**, R603 (2004).
- [34] B. Dieny, S. Sankar, M. R. McCartney, D. J. Smith, P. Bayle-Guillemaud, and A. E. Berkowitz, Spin-Dependent tunneling in discontinuous metal/insulator multilayers, *J. Magn. Magn. Mater.* **185**, 283 (1998).
- [35] G. Fahsold, A. Pucci, and K.-H. Rieder, Growth of Fe on MgO(001) studied by He-atom scattering, *Phys. Rev. B* **61**, 8475 (2000).
- [36] D. Apalkov, B. Dieny, and J. M. Slaughter, Magnetoresistive random access memory, *Proc. IEEE* **104**, 1796 (2016).
- [37] H. X. Yang, M. Chshiev, B. Dieny, J. H. Lee, A. Manchon, and K. H. Shin, First-Principles investigation of the very large perpendicular magnetic anisotropy at Fe|MgO and Co|MgO interfaces, *Phys. Rev. B* **84**, 054401 (2011).
- [38] T. Burkert, O. Eriksson, P. James, S. I. Simak, B. Johansson, and L. Nordström, Calculation of uniaxial magnetic anisotropy energy of tetragonal and trigonal Fe, Co, and Ni *Phys. Rev. B* **69**, 104426 (2004).
- [39] T. Burkert, L. Nordström, O. Eriksson, and O. Heinonen, Giant Magnetic Anisotropy in Tetragonal FeCo Alloys, *Phys. Rev. Lett.* **93**, 027203 (2004).
- [40] P. Bruno, Tight-Binding approach to the orbital magnetic moment and magnetocrystalline anisotropy of transition-metal monolayers, *Phys. Rev. B* **39**, 865 (1989).
- [41] Y. Miura, S. Ozaki, Y. Kuwahara, M. Tsujikawa, K. Abe, and M. Shirai, The origin of perpendicular magnetocrystalline anisotropy in $L1_0$ -FeNi under tetragonal distortion, *J. Phys. Condens. Matter.* **25**, 106005 (2013).
- [42] J. Zhang, P. V. Lukashev, S. S. Jaswal, and E. Y. Tsybal, Model of orbital populations for voltage-controlled magnetic anisotropy in transition-metal thin films, *Phys. Rev. B* **96**, 014435 (2017).
- [43] V. Popescu, H. Ebert, B. Nonas, and P. H. Dederichs, Spin and orbital magnetic moments of 3d and 4d impurities in and on the (001) surface of Bcc Fe, *Phys. Rev. B* **64**, 184407 (2001).
- [44] G. van der Laan, Microscopic origin of magnetocrystalline anisotropy in transition metal thin films, *J. Phys. Condens. Matter.* **10**, 3239 (1998).